Physics of Fluids

RESEARCH ARTICLE | FEBRUARY 04 2025

Experimental study on the flow field inside soap bubble at different incident velocities

Qingkai Zhao (赵庆凯); Zhixuan Yang (杨智轩); Wei Xiao (肖魏); Ying Li (李颖); Yat Sze Choy (蔡逸思)

Check for updates

Physics of Fluids 37, 023315 (2025)
https://doi.org/10.1063/5.0250579

View Online

Export Citation

Articles You May Be Interested In

Unblowing bubbles: Understanding the physics of bubble deflation through a straw

Am. J. Phys. (October 2025)

Formation of soap bubbles by gas jet

Appl. Phys. Lett. (December 2017)

Soap bubbles in paintings: Art and science

Am. J. Phys. (December 2008)

AIP Publishing

Physics of Fluids ARTICLE pubs.aip.org/aip/pof

Experimental study on the flow field inside soap bubble at different incident velocities

Cite as: Phys. Fluids **37**, 023315 (2025); doi: 10.1063/5.0250579
Submitted: 26 November 2024 · Accepted: 5 January 2025 ·
Published Online: 4 February 2025

Qingkai Zhao (赵庆凯),[1] Zhixuan Yang (杨智轩),[2] Wei Xiao (肖魏),[2] Ying Li (李颖),[1,a)] and Yat Sze Choy (蔡逸思)[1,a)]

AFFILIATIONS

[1]Department of Mechanical Engineering, The Hong Kong Polytechnic University, Hong Kong, China
[2]College of Shipbuilding Engineering, Harbin Engineering University, Harbin 150001, China

[a)]Authors to whom correspondence should be addressed: carlos.li@connect.polyu.hk and yatsze.choy@polyu.edu.hk

ABSTRACT

Bubbles are widely present in nature. However, previous scientific studies have primarily focused on the development of the outer contour of the bubble while neglecting the changing behavior of the internal flow field due to the difficulty in implementing experiments. This study designs a simple experimental device that can conveniently observe changes in the flow field inside the bubble while avoiding the tedious operation and high costs associated with the particle image velocimetry (PIV) system. Accordingly, this experiment investigates the development process of the flow field inside the bubble and the velocity conditions required for bubble formation for different incident velocities and Reynolds numbers. The study first examines the minimum flow velocity necessary for bubble formation. Then, under low-speed conditions, the flow inside the straw is laminar, and the flow field inside the bubble exhibits a single vortex structure. Under high-speed conditions, the flow inside the straw transitions to turbulent flow, and the flow field inside the bubble exhibits a four-vortex structure. The formation process of this four-vortex structure shows variations as the flow velocity increases. In addition, this study proposes corresponding physical models for bubble formation under low and high flow velocities and verifies the models.

I. INTRODUCTION

Bubbles are widely present in various applications, including marine structures,[1–3] medical,[4–8] chemical industry,[9–12] and agriculture,[13] and they have a significant impact on structural stability[14–17] and flow field stability.[18–20] Hence, scientific researchers have studied bubbles for a long time.

Early research primarily focused on the physical processes of bubble expansion and collapse. Plesset and Chapman[21] investigated the collapse of a spherical bubble near a solid boundary. Lauterborn and Bolle[22] experimentally validated Plesset and Chapman's work and measured bubble growth rates. Li *et al.*[23] tracked bubbles in a Venturi tube, identifying different development stages through pressure pulsation signals. Lindau and Lauterborn[24] used lasers to generate bubbles and utilized high-speed cameras to document bubble development and collapse, examining the effects of wall boundary conditions on bubble dynamics. At this stage, with limited computer technology availability, simulation research on bubbles primarily centered on mathematical methods. Kermeen *et al.*[25] proposed a fully relaxed numerical solution for axisymmetric cavitation flow and validated the method using prior experimental results. Blake and Gibson[26] applied the boundary element method to solve the Laplace equation, clarifying the development of bubbles near solid boundaries. Robinson and Blake[27] developed a boundary integral method to calculate bubble development under the assumptions of inviscid and incompressible fluids, confirming its accuracy through experiments.

Due to the rapid development of industry, bubbles appear increasingly frequently in various fields, and the associated situations are becoming more complex. Therefore, researchers have investigated various environmental conditions that produce cavitation bubbles and proposed more accurate bubble models. Zhang and Liu[28] improved the traditional boundary element method and utilized grid-adaptive technology to calculate the development process of bubbles generated during underwater explosions. Hanke and Metzler[29] examined bubbles in DNA and explained the formation mechanism of local denaturation areas in double-stranded DNA. Zhou *et al.*[30] investigated the bubble development process in a gas–liquid bubbling tower and observed the bubble changes when multiple bubbles clustered. Mettin *et al.*[31] analyzed the process of cavitation bubble generation under ultrasonic action, observed changes in bubble radius over time, and used empirical formulas to fit the bubble development process. Huang *et al.*[32] explored the bubbles generated when a sphere enters the water from the air. The researchers established a cavity dynamics model for water entry based on the theory of incompressible potential flow and verified the model's accuracy through experiments. Xiao *et al.*[33] refined the bubble model and developed a bubble model under compressible fluid conditions using the boundary integral method. This model effectively calculates the development process of annular bubbles during the bubble collapse stage. Phan *et al.*[34] used a high-energy laser to generate bubbles and investigated the effect of temperature on the bubble development process. Shen *et al.*[35] developed a bubble model that takes into account the viscosity of the liquid. Huber *et al.*[36] created a model of bubbles that slowly precipitate from magma during volcanic eruptions based on the lattice Boltzmann method of free surface flow. This model innovatively considers the mass exchange between the bubble and the surrounding environment during its development, and its accuracy is verified through experimental comparisons. Straub[37] investigated the development of bubbles in microgravity, while Zhong and Ardekani[38] examined bubbles in protein solutions and modeled the bubbles under the conditions of protein solubility and bubble surface tension.

The above studies focus more on developing bubble boundaries, while the development process inside the bubble is still relatively underexplored. This limitation is related to the difficulty of observing the flow field inside the bubble. However, only a few researchers have studied this direction. Ahmed and Erath[39] explored the flow field structure inside a semi-enclosed cavity when the piston moves vertically at high speed. Rao *et al.*[40] utilized a special nozzle to study the flow field inside the bubble at a fixed jet velocity. Since the flow field inside the bubble significantly influences the bubble's development process. The vortex structure inside the bubble is likely to be related to the noise.[41–44] At the same time, studying the flow field inside the bubble helps researchers understand the pressure distribution inside the bubble, which may help the development of some new soft robots.[45,46] The flow field inside the bubble has many similarities with the blood distribution inside the heart,[47] so this research will also be beneficial to the development of artificial hearts, so further research is conducted. A set of equipment is designed to observe the flow field inside the bubble in the air. Several incident airflows with different speeds are set, the modes of the flow field inside the bubble at various speeds are observed, and a corresponding bubble flow field model is proposed based on these observations.

II. EXPERIMENTAL METHOD

A. Experimental equipment

A set of equipment was developed for observing changes in the flow field of bubbles in this experiment. Compared to the traditional PIV (particle image velocimetry) system, this device provides better observation results, lower experimental costs, and a more compact equipment scale, making it convenient for conducting experiments. Figure 1 illustrates the schematic diagram of this experimental system:

The components in Fig. 1 are as follows: 1 is the control system, which primarily controls the high-speed camera and processes the images captured by the high-speed camera; 2 is the high-speed camera, specifically a Phantom VEO-710S high-speed camera; 3 is the laser light strip. Since this experiment is conducted in a camera darkroom and the laser light strip is long, it is considered a plane light; 4 is a small air compressor providing gas with a certain initial pressure; 5 is a one-way solenoid valve that controls the gas outflow; 6 is a small combustion chamber filled with refined tobacco, with another one-way solenoid valve installed on the left side of the combustion chamber; 7 is an air chamber used to mix the gas, and an observation window is installed on its side to verify whether the gas is fully mixed easily; 8 is the single switch with a pressure gauge; 9 is an MS56EC medical single-channel syringe pump with an injection accuracy of 2%. The syringe pump can also automatically identify 20 to 80 ml syringes. In this experiment, an 80 ml syringe was used when the injection speed exceeded 18 m/s, and a 20 ml syringe was selected when the injection speed was below this threshold. This ensured that a complete bubble could be formed after increasing the injection speed; 10 is a pneumatic switch, and its specific use is depicted in Fig. 2. In addition, Fig. 2 shows the detailed schematic diagram of the section enclosed by the dotted line in Part A: 1 of Fig. 2.

A high-precision medical syringe pump (9 in Fig. 1) was utilized in this experiment to ensure a constant gas flow rate entering the

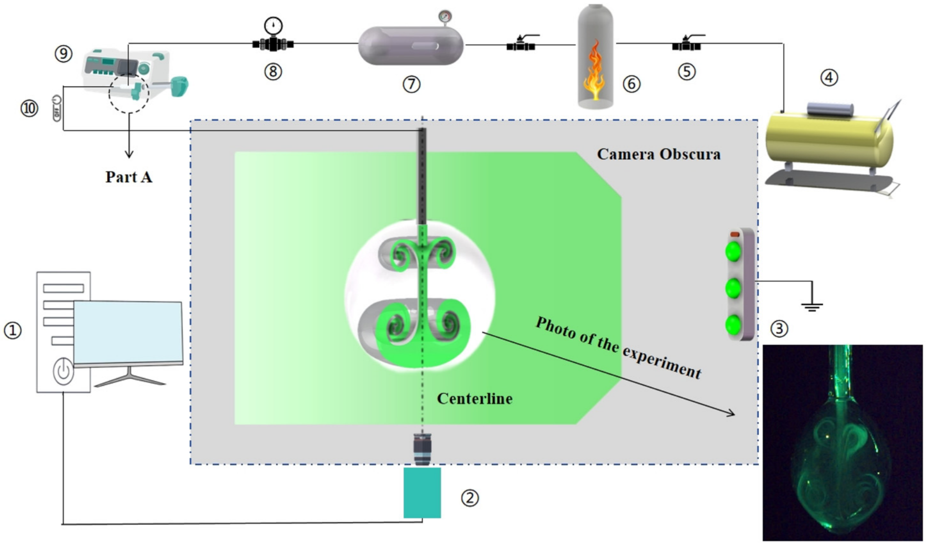

FIG. 1. Schematic diagram of the experimental system.

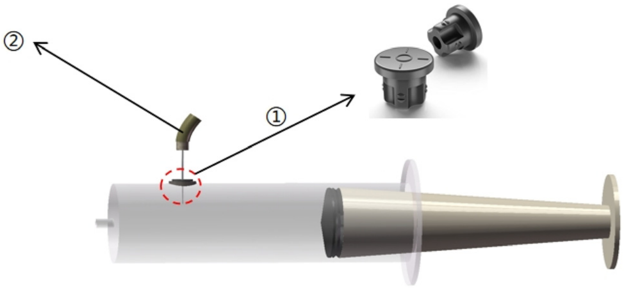

FIG. 2. Schematic diagram of syringe connection (Part A of Fig. 1).

bubble. A pneumatic switch (10 in Fig. 1) was installed before the syringe pump to ensure the syringe pump dispenses the mixed gas only after the syringe is filled with the mixed gas. The parts in Fig. 2 are as follows: 1 is a self-healing rubber stopper with a diameter of 10 mm, connected to the syringe with superglue; 2 is the rubber tube used in this experiment, with an inner diameter of 2 mm and a wall thickness of 0.4 mm.

At the beginning of the experiment, 10 is in the closed state, and the fully mixed gas in 7 enters the syringe through the self-healing rubber stopper. At this stage, the syringe pump is inactive. Once the syringe is filled with the mixed gas, 10 is opened, and the needle is removed from the rubber stopper. Then, the bubble observation can commence. The laser beam in this experiment aligns coplanar with the bubble's maximum diameter section and the straw's midline employed to blow the bubble. The diagram is shown in Fig. 3:

Figure 3 indicates that compared to the PIV system, this experimental equipment conveniently observes the internal flow field on each cross section inside the bubble, implements the experiment more efficiently, and avoids the tracer particle superposition problem that often occurs in the PIV system.

The thin tobacco used in this experiment was Kentucky 3R4F. The tobacco was stored for 50 h in an environment with a temperature of 22 °C and a humidity of 58% before being placed in the combustion chamber. The solenoid valve of the combustion chamber was not opened until the tobacco was fully burned. The average diameter of the smoke particles produced by this type of tobacco after combustion is about 250 nm, based on the research of Zhao *et al.*[48] In addition, the density of the mixed gas used in this experiment is $1.42\,\mathrm{kg/m^3}$ at a temperature of 22 °C; the surface tension coefficient of the soap solution measured by the pull-off method is 72 mN/m; the dynamic viscosity coefficient of the mixed gas, obtained using the Sutherland formula, is $41.9\,\mu\mathrm{P_a}\cdot\mathrm{s}$.

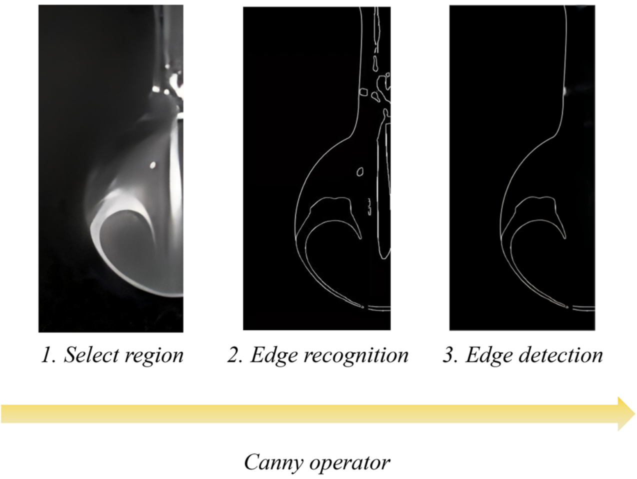
1. Select region 2. Edge recognition 3. Edge detection

FIG. 4. Extraction process of bubble boundaries.

B. Bubble boundary extraction method

The images obtained by high-speed cameras are often affected by factors such as light and refractive index. Simultaneously, the objects photographed must be quantified. Therefore, many scholars use various image processing methods to process these images.[49,50] This study adopts and optimizes the bubble contour extraction procedure used by Zhao *et al.*[51]

Figure 4 shows that in this experiment, a relatively small area that must be identified was selected to minimize the impact of noise. This area includes the bubble boundary and the vortex structure inside the bubble. After recognition, the many discontinuous segments inside the bubble were removed. This experiment established the following two recognition criteria to remove these discontinuous points:

a. The curve with the longest number of continuous pixels is the outermost contour of the bubble.
b. The curve with the longest continuous closed pixels is the vortex structure inside the bubble.

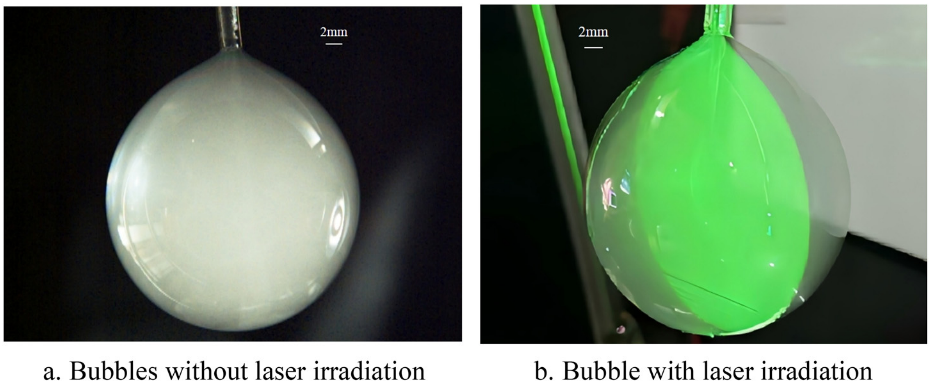

a. Bubbles without laser irradiation b. Bubble with laser irradiation

FIG. 3. Comparison of bubbles with and without laser irradiation.

Another issue that must be considered is adding a coordinate system to the recognized contour. The conversion relationship is as follows:

$$\lambda = \frac{L_{real}}{L_{criterion}}, \tag{1}$$

$$L_{\mathrm{real}} = \lambda L_{picture}, \tag{2}$$

where L_{picture} is the size in the picture, $L_{\mathrm{criterion}}$ is the standard size in this experiment, and λ is the ratio of the two. The real size (L_{real}) corresponding to any size in the picture can be calculated by applying this ratio and Eq. (2). This experiment has two standard sizes. The horizontal standard size is the diameter of the plastic hose, which is 2.8 mm. The vertical standard size is the length of the plastic hose, which is 5 mm in this experiment. Figure 5 provides a coordinate diagram based on the above principle.

C. Parameters of the vortex structure

This section outlines the necessary parameters for studying the vortex. The parameter details are shown in Fig. 6.

Figure 6(a) indicates that the vortex's center point, (X_r, Y_r), is visible in this experiment. The center point is the location where the streamlines of the vortex disappear. The experiment was repeated five times for each Reynolds number to ensure the accuracy of the center point coordinates. The final center point coordinate is the average of the five center point coordinates. V_y is the gas flow rate from the straw into the bubble, and the dotted line on the far right is the centerline of the incident airflow.

Figure 6(b) illustrates that the vortex structure's separation point is the closest to the center point. As the bubble's bottom deflects the incident airflow, it forms the outermost layer of the vortex structure at the separation point and gradually evolves into a multi-layer vortex structure. Additionally, this experiment defines the maximum length (R_y) and width (R_x) of the vortex structure. Furthermore, this experiment defines other parameters related to the bubble, as depicted in Fig. 7.

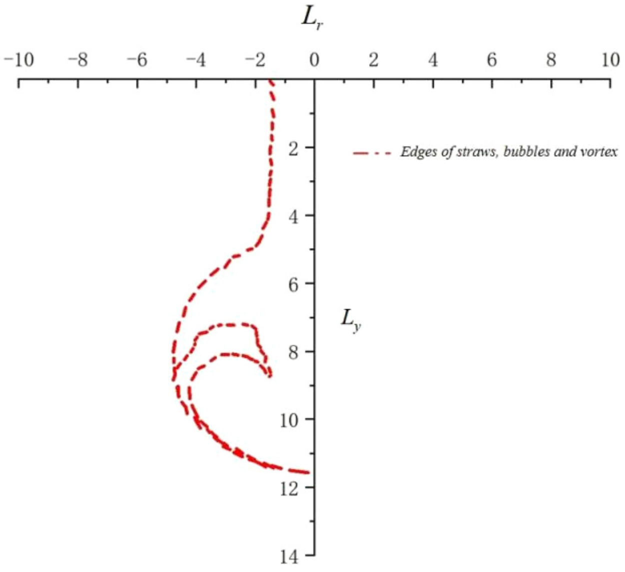

FIG. 5. Schematic diagram after adding coordinate system.

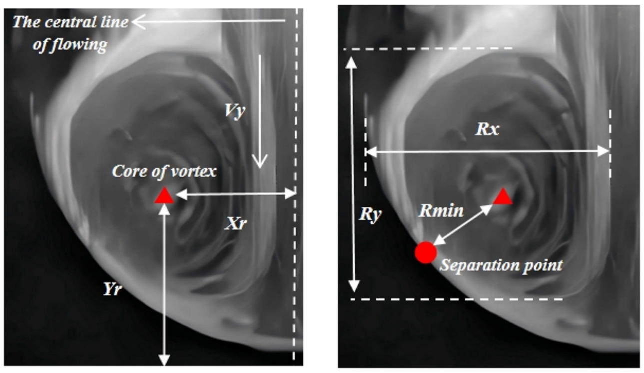

a. Definition of the vortex's core

b. Definition of the separation point

FIG. 6. Definition diagram of the parameters of the vortex.

Figure 7 shows the bubble's front view on the left and its top view on the right. It provides definitions for a series of parameters, such as the bubble radius and the straw's inner and outer diameters.

III. RESULTS AND ANALYSIS

A. Conditions for forming bubbles

Bubbles can form as the gas jet acts on the liquid film. The liquid film deforms under the combined influence of gas pressure and surface tension and eventually forms bubbles. Salkin *et al.*[52] and Zhou *et al.*[53] proposed respective models for this process. This section verifies these models and introduces some improvements. The calculation formula for the Reynolds number in the pipe is as follows:

$$R_e = \frac{\rho u d}{\mu}. \tag{3}$$

The gas dynamic viscosity coefficient at room temperature is 41.9 $\mu\mathrm{P_a} \cdot \mathrm{s}$ in this experiment. After calculation, it is determined that

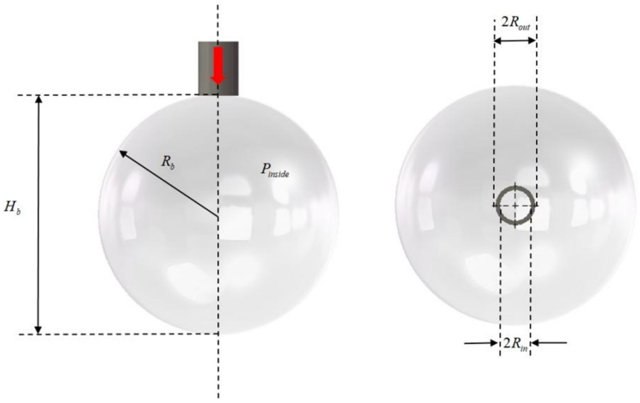

FIG. 7. Schematic diagram of the bubble parameter definition.

$R_e < R_{e\sigma}$ $R_e < R_{e\sigma}$, where $R_{e\sigma}$ the critical Reynolds number indicates that the flow in the pipe during this experiment is laminar.

This study adopts the model proposed by Salkin *et al.*[52] and Zhou *et al.*,[53] which states that the condition for bubble generation occurs when the pressure of the gas jet equals the Laplace pressure of the liquid film. The formula can be described as follows:

$$\frac{1}{2}\rho_g v_c^2(\delta) = 4\gamma/R, \tag{4}$$

where ρ_g is the density of the gas, δ is the distance from the gas nozzle to the soap film, $v_c(\delta)$ is the gas jet velocity at δ, γ is the surface tension coefficient of the bubble film, and R is the radius of the bubble, representing the radius of curvature in this study. When $R = R_{in}$, bubbles begin to form.

In this experiment, the flow in the pipe is laminar, and the distance between the straw and the soap film is zero. In addition, Eq. (4) does not account for friction losses along the gas flow in the pipeline; therefore, it requires modification to some extent. The parameters and flow in the circular tube are expressed in Fig. 8:

Based on Darcy's,[54] the friction loss along a laminar flow in a circular tube can be described as follows:

$$\Delta p = \lambda \cdot \frac{l}{d} \cdot \frac{\rho v^2}{2}, \tag{5}$$

where λ is the frictional resistance coefficient, which can be expressed by the following formula:

$$\lambda = \frac{64}{R_e}. \tag{6}$$

Then, Eq. (4) can be written as follows:

$$\frac{1}{2}\rho_g v_c^2 + \Delta p = 4\gamma/R_{\mathrm{in}}. \tag{7}$$

The formula for critical velocity is derived by substituting Eqs. (5) and (6) into (7) and rearranging them as follows:

$$v_c = \frac{2\sqrt{\left(16\mu^2 l^2 + 2\rho\gamma R_{in}^3\right)} - 8\mu \mathrm{l}}{R_{in}^2 \rho}. \tag{8}$$

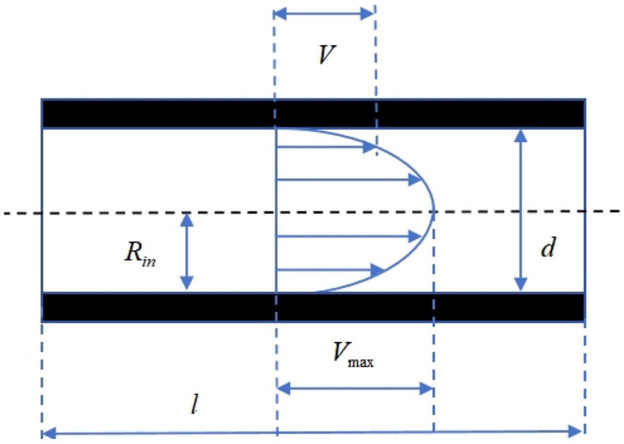

FIG. 8. Schematic diagram of flow in the pipeline.

Accordingly, Eq. (8) constitutes a condition for bubble formation, representing the minimum velocity required. Equation (8) approximately determines that $v_c \sim \frac{1}{\sqrt{R_{in}}}$, which aligns with the research findings of Salkin *et al.*[49] and Zhou *et al.*[50]

The experiment used several plastic hoses with radii of 1, 2, 4, 6, 8, and 10 mm for verification of the accuracy of this conclusion. The results are as follows:

Figure 9 indicates that the attenuation trend of the critical velocity in the existing model is gentler within a specific pipeline radius range, indicating that the calculation results are closer to the experimental data.

When the bubbles are generated, the expansion speed of the bubbles is not constant. The experiment employed TEAM software to track the movement of the bubble apex and conduct an in-depth study of this phenomenon. Figure 10 provides a schematic diagram of the bubble apex and briefly introduces the working principle of TEAM software.

Figure 10 reveals that TEMA software marks a specific point in the experimental image and determines the moving speed of the marked point based on the time interval of high-speed imaging and the moving distance of the specific point.

Figure 11 indicates that the speed of the tracking point undergoes a small amplitude oscillation process and eventually stabilizes near a certain speed, which is slightly lower than the speed displayed by the injection pump (the bubble injection speed in Fig. 11 is 14 m/s). After analysis, this phenomenon is attributed to two factors: a certain amount of friction loss within the pipe itself and the elastic nature of the liquid film at the pipe port, which reduced the speed of the jet.

The oscillations observed in Fig. 11 is mainly caused by the roughness of the nozzle cross section, the adhesion of the pipe's inner wall, and the surface tension of the liquid film. Around $t = 0.018$ s, the bubble appeared to be "stuck," meaning the bubble's development speed suddenly decreased. Then, under the strong push of the following jet, the bubble "overcame" this resistance. At this point, the acceleration of the liquid film pointed outward from the nozzle, causing the

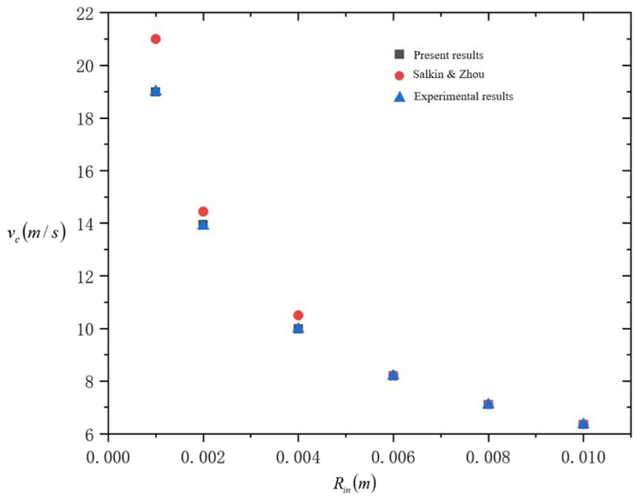

FIG. 9. Comparison of critical speeds corresponding to different R_{in} calculated using different models and experimental results.

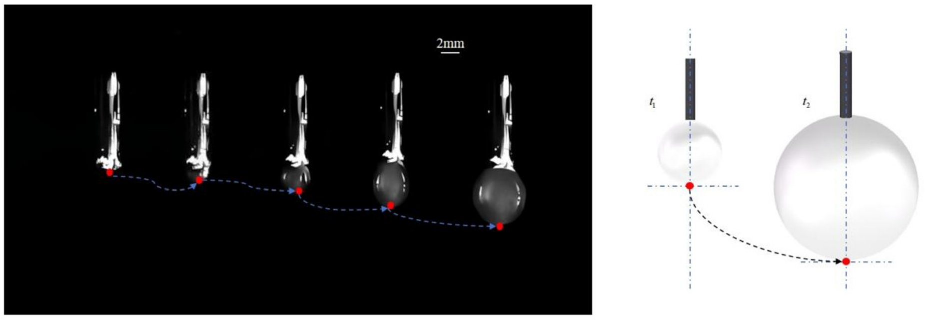

a. Experimental Results b. Tracking point diagram

FIG. 10. Schematic diagram of tracking points and experimental results.

bubble to suddenly stretch around $t = 0.03$ s. This resulted in the bubble transitioning from a perfect circle to an ellipse with a long axis. Then, the elasticity of the bubble's liquid film buffered the downward acceleration, allowing the bubble to develop with small oscillations. This development resembled a damped vibration, ultimately causing the bubble shape to stabilize near a perfect circle.

This experiment also measured the velocity change curves of the bubble tracking point at several other initial velocities. The results are as follows:

Figure 12 reveals that the speed curves of the tracking points at the four velocities exhibit roughly similar trends, with all curves tending to stabilize after experiencing small amplitude oscillations. However, differences in the initial speed result in subtle variations in the speed changes of the tracking point. First, the point where the tracking point becomes "stuck"-gradually advanced (indicated by the red dot in the figure, with the red dotted line and arrow approximating the red dot's progression). Second, the oscillation stage experienced by the bubble initially increases and then decreases as the speed rises, peaking at $v = 18$ m/s before rapidly decreasing. This indicates that when $v > 18$ m/s, the jet speed is sufficiently high that the surface tension of the liquid film and the adhesion of the circular tube wall have less impact.

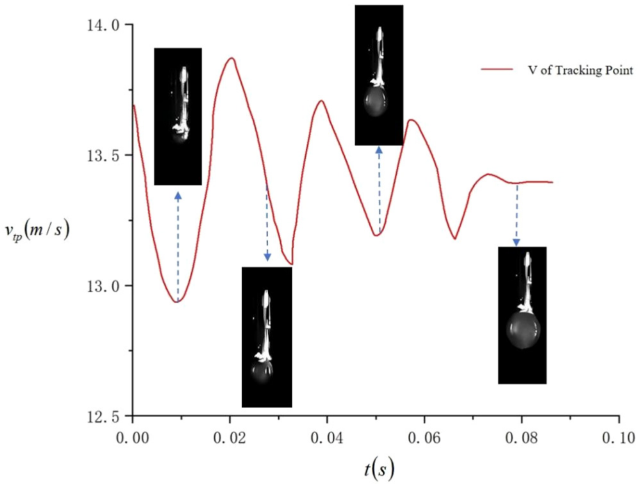

FIG. 11. Speed curve of the tracking point.

B. The vortex inside the bubble at a low flow speed

This experiment set different incident velocities: 22, 20, 18, 16, and 14 m/s. It was observed that when the incident velocity was low ($V_y < 18$ m/s), the Reynolds number was lower than the critical Reynolds number, and the bubble exhibited a single vortex structure. When the incident velocity was high ($V_y > 18$ m/s), the Reynolds

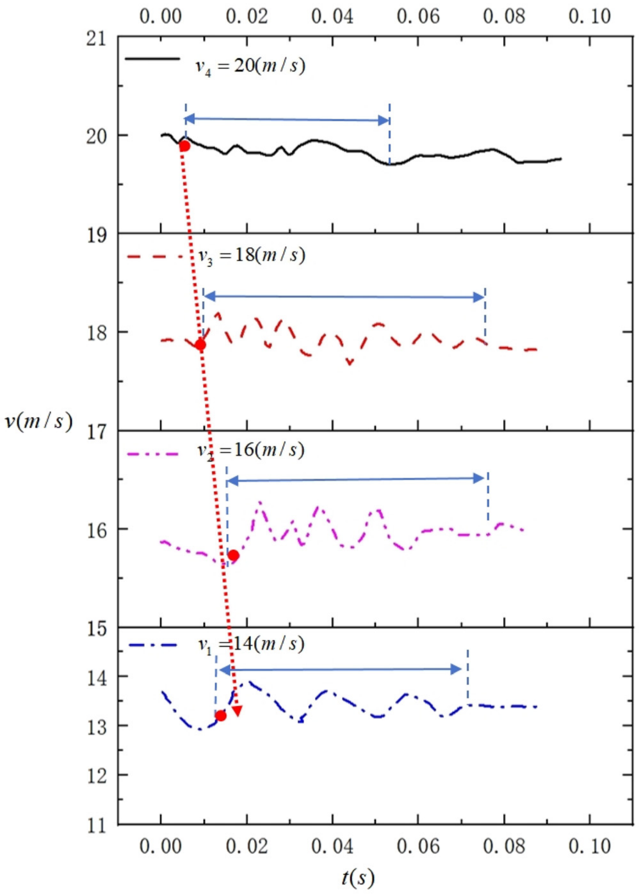

FIG. 12. Tracking point velocity at the initial stage of bubble development at several speeds.

number exceeded the critical Reynolds number, and the bubble exhibited a four-vortex structure. When the incident velocity reached 18 m/s ($V_y = 18\,\text{m/s}$), the Reynolds number was approximately equal to the critical Reynolds number, causing the bubble to transition from a single vortex structure to a double vortex structure. Each speed scenario was repeated fifty times in the experiment. This section discusses the case when $v < 18\,\text{m/s}$.

Figure 13 indicates that a single vortex structure formed within the air bubble in the slow state. Figure 13(a) exhibits that the airflow enters the air bubble through the straw, and the air bubble gradually forms. Because the density of the mixed airflow was low, the expansion speed of the air bubble was slower. Hence, the mixed airflow did not rush down along the diameter but instead moved along the edge of the bubble, gradually spreading along its wall surface. This phenomenon appeared to be related to the sedimentation of fine smoke particles from the mixed gas onto the bubble wall. As more gas entered the bubble, this sedimentation weakened. Figures 13(b)–13(d) indicate that the mixed gas entering the bubble formed a smaller angle with the bubble. After a significant amount of gas entered, the mixed gas was pushed to continue moving along the bubble wall, eventually forming a single vortex structure, as shown in Figs. 13(e)–13(f).

Figures 13(c) and 13(d) depict the process of vortex formation, whereas Fig. 14 provides more detailed experimental images:

Figure 14 indicates that this study utilizes a program to extract the edge line of the vortex structure and position it beside the original image, represented by the blue arrow line in Fig. 14. It is evident from the distribution and direction of the blue line that as the gas gradually enters the bubble, some gas deposits at the bottom of the bubble. This

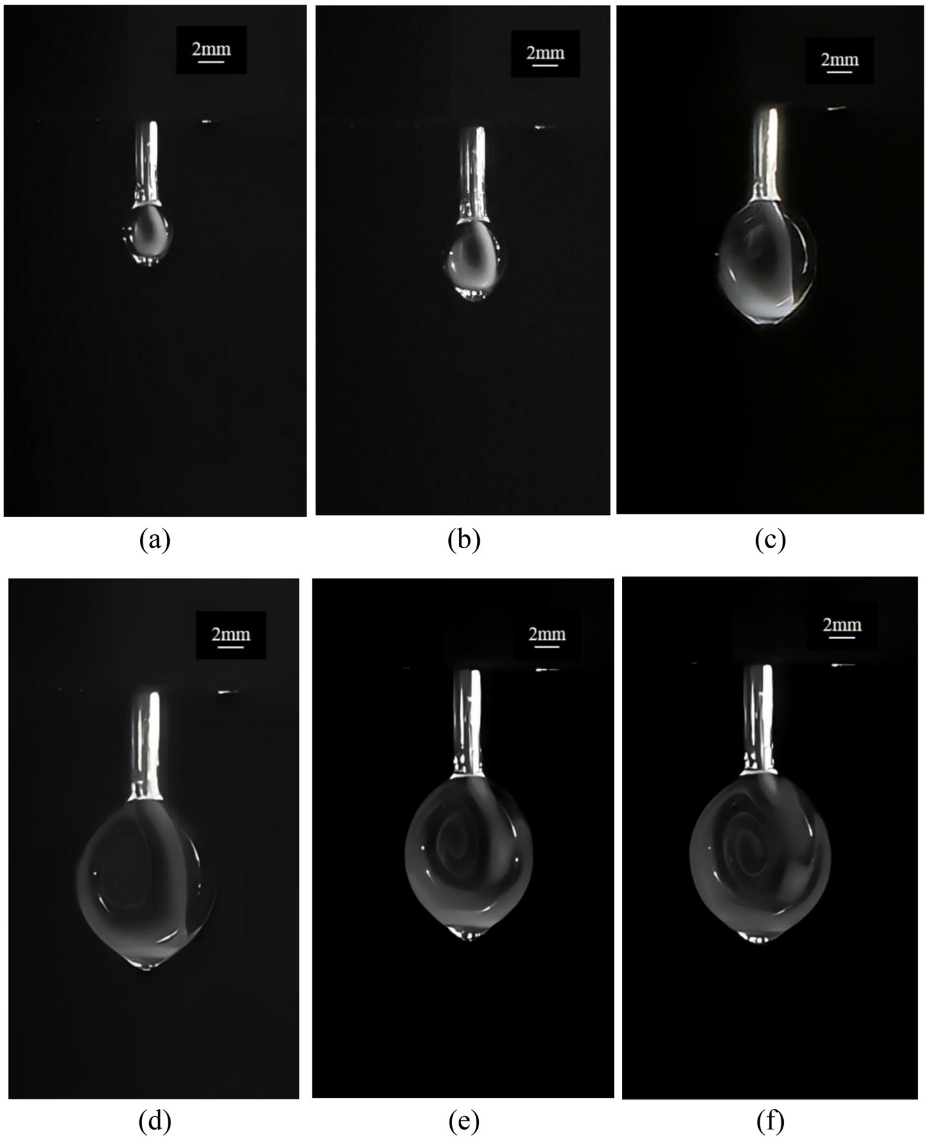

FIG. 13. In the low-speed state, the internal vortex structure development process of the air bubble (take $V = 14\,\text{m/s}$ as an example).

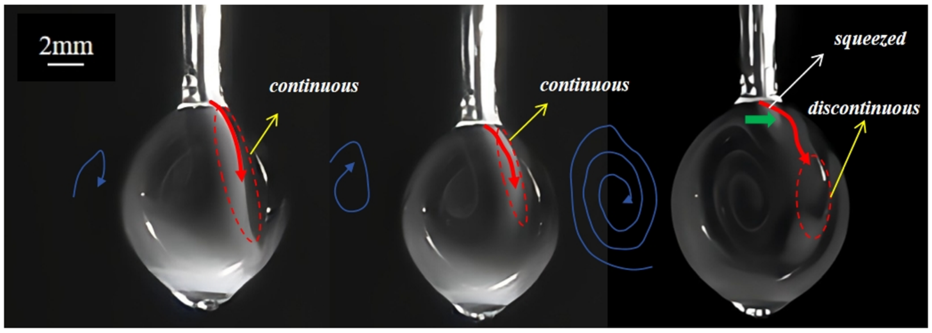

FIG. 14. Schematic diagram of the formation process of vortex.

portion of the gas is pushed by subsequent gas to move along the bubble wall toward the upper part of the bubble. After reaching a specific position, the gas gradually forms a more distinct vortex structure.

As the vortex structure develops, the velocity at the center is low, while the linear velocity at the outer edge is high. This vortex directs the mixed gas entering the bubble at a certain angle closer to the bubble wall, causing the section outlined by the dotted line in Fig. 14 to gradually shorten until it completely breaks, as shown in the rightmost image of Fig. 14. Simultaneously, observations reveal that the vortex absorbs a significant amount of gas initially deposited at the bottom of the bubble, ensuring that all the gas inside the bubble remains in motion. This makes the tube side of the bubble clearer, and the bubble itself approximates a perfect circle.

The experiment also investigated the angle between the incident airflow and the vertical direction, which correlates with the velocity of the incident gas. First, this experiment defines this angle as follows:

Figure 15 indicates that θ is the angle between the centerline of the bubble and the tangent line at the top of the gas jet edge line. Figure 15 illustrates bubbles at $t = 0.12$ s, where the incident velocity in Fig. 15(a) is $v = 14$ m/s, and the incident velocity in Fig. 15(b) is $v = 16$ m/s. The angle θ in Fig. 15(a) is larger than that in Fig. 15(b); therefore, as the incident airflow velocity increases, the mixed gas entering the bubble gradually approaches the centerline of the bubble. Another phenomenon is that as the incident airflow velocity increases, the bubble's vortex continuously compresses the airflow, deflecting its direction and moving it closer to the bubble wall.

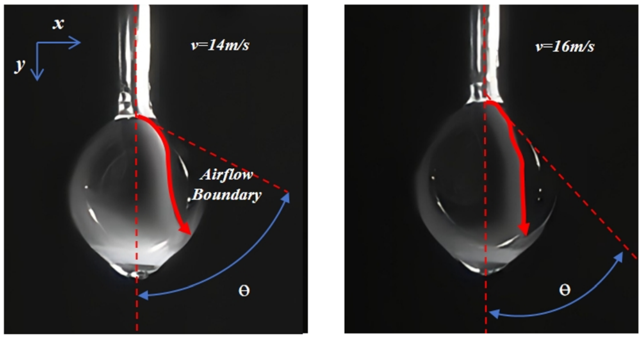

(a) (b)

FIG. 15. Schematic diagram of the angle between the gas jet and the centerline.

This experiment tracked the boundary change process of the incident gas within the bubble from $t = 0.03$ to 0.21 s to explore the variation of this angle.

Figure 16 demonstrates that the boundary of the incident airflow changes as the vortex structure evolves during bubble development. This experiment categorizes the angle change process into three stages: "Increase, Collapse, and Re-increase." When the mixed gas initially enters the bubble, it gradually diffuses along the bubble wall. As more mixed gas enters, a vortex structure forms, causing the linear velocity of the gas boundary to increase, the pressure to decrease, and the newly entered gas to be "attracted." Therefore, the incident angle shifts toward the bubble's central axis, representing the "Collapse" stage. As the vortex structure develops, its rotation forces the incident airflow to diffuse along the bubble wall again, marking the "Re-increase" stage.

At different incident speeds, the duration of these three stages varies. Figure 16 shows that when the incident speed is 16 m/s, the initial "Increase" stage experienced by the bubble is shortened, indicating that the vortex develops more rapidly and the incident airflow is "absorbed" by the vortex earlier. Simultaneously, the "Collapse" and "Re-increase" stages are relatively longer, resulting in a larger final bubble size.

This experiment accurately identified the angle between the incident airflow and the bubble's central axis using the boundary recognition program. The angle variation is presented in Fig. 17.

Figure 17 exhibits that the blue angle in the left diagram represents the angle change in the "Increase" stage, the red angle represents the angle change in the "Iollapse" stage, and the green angle represents the angle change in the "Re-increase" stage. In addition, the longer one side of the angle is, the later the angle appears. The scatterplot on the right illustrates the angle change process more clearly. At different speeds, the incident airflow angle demonstrates a trend of initially increasing, then decreasing, and finally increasing again. However, the first increase stage is shorter at higher speeds, while the decrease and re-increase stages are longer.

This experiment analyzed the vortex's center point and development radius change process utilizing the identification procedure, and the results are illustrated in Fig. 18.

Figure 18 indicates that the vertical axis (the z-axis) represents time, corresponding to the time nodes in Fig. 16. When identifying all the coordinates in Fig. 18, the center point at the end of the straw is

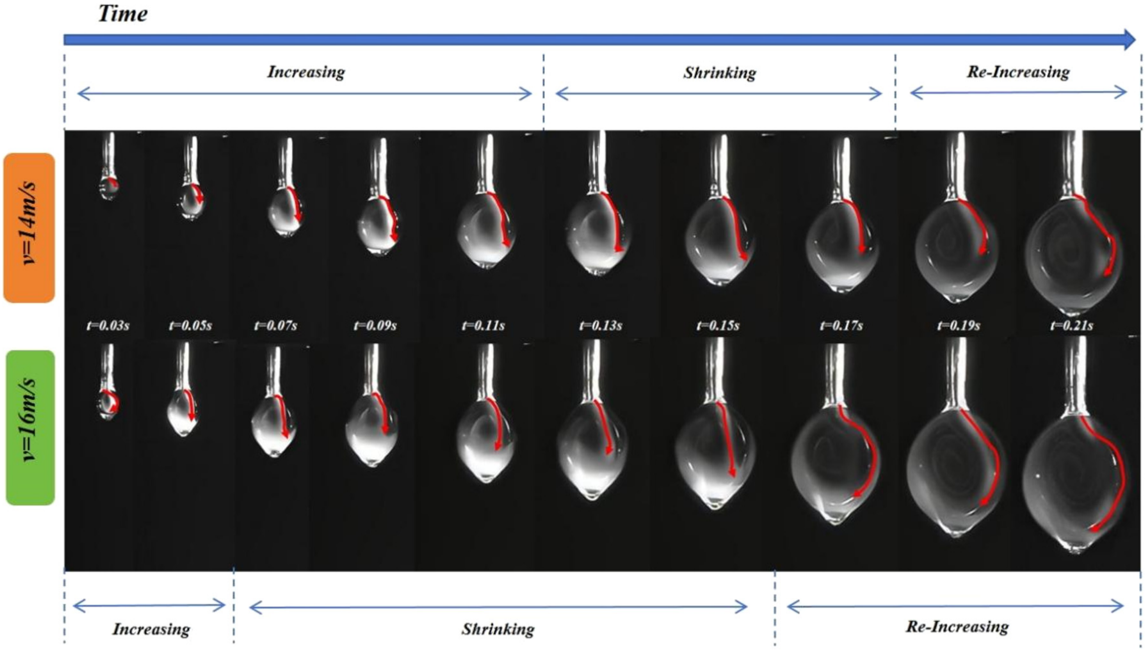

FIG. 16. Incident airflow profiles at different speeds.

the coordinate origin. Bubbles' geometric center remains approximately near a straight vertical line, exhibiting uniform expansion. For the vortex structure, during the initial stage of bubble generation, the vortex center point nearly coincides with the bubble's center point, consistently remaining around the bubble's geometric center. As the bubble expands, the vortex center separates from the bubble center, influenced by the precipitation of mixed gas at the bubble's bottom and the interaction between the incident airflow and the vortex structure. The projection of this figure on the z-y plane illustrates this process more clearly.

In addition, the incident airflow did not only form rightward vortices but occasionally rotated leftward during the experiment.

Figure 19 depicts the experimental results of a left-handed vortex at varying speeds for a straw with an inner diameter of 2 mm.

This experiment recorded the frequency of left-hand and right-hand rotations of mixed gases in straws with different diameters at low speeds. The results are presented in Table I.

This experiment was repeated fifty times under each pipe diameter condition, and the number of left-hand and right-hand rotations was counted. Table I shows that the ratio of left-hand to right-hand rotations is approximately 1:1. This indicates that the mixed gas is in an unstable state after entering the bubble, and the probability of left-hand and right-hand rotations is nearly equal, which aligns with the jet instability observed in the experiment by Rao *et al.*[40]

Few theoretical models correspond to vortex structures at low speeds. The basic vortex dynamic equation involves the pressure at each point in the vortex structure, which is extremely challenging to measure in experiments. Therefore, this experiment proposes a new, simpler model to approximate the growth process of bubbles. In this derivation, the bubble is assumed to be approximately a perfect sphere, and the thickness of the straw is ignored. The parameters required for this model are illustrated in Fig. 7.

The bubble in this experiment is approximated as spherical cap geometry, allowing its volume to be calculated by integration.

$$V = \frac{\pi h\left(3R_{in}^2 + h^2\right)}{6}, \tag{9}$$

where h is the height of the spherical cap, $h = 2R_b - H_b$. Differentiating both sides of Eq. (9) yields the rate of change of volume over time, i.e., the volume flow rate Q is as follows:

$$Q = \frac{dV}{dt} = \frac{\pi\left(R_{\text{in}}^2 + h^2\right)}{2} \cdot \frac{dh}{dt} = v \cdot \pi R_{\text{in}}^2. \tag{10}$$

The expression of v is given in Eq. (8). The following relationship is derived using Eq. (10):

$$\frac{dh}{dt} = \frac{4\left(\sqrt{16\mu^2 l^2 + 2\rho\gamma R_{\text{in}}^3} - 4\mu l\right)}{\rho\left(R_{\text{in}}^2 + h^2\right)}. \tag{11}$$

At this point, the rate of change of the spherical crown height over time is calculated, but this formula is overly complicated. The term $2\rho\gamma R_{\text{in}}^3$ is ignored to simplify Eq. (11) as follows:

$$\frac{dh}{dt} = \frac{A}{R_{\text{in}}^2 + h^2}, \tag{12}$$

where $A = \frac{4\left(\sqrt{16\mu^2 l^2 + 2\rho\gamma R_{\text{in}}^3} - 4\mu l\right)}{\rho}$. Therefore, the relationship between h and t can be obtained by integration of Eq. (12)

$$h^3 + 3R_{\text{in}}^2 h - 3At = 0. \tag{13}$$

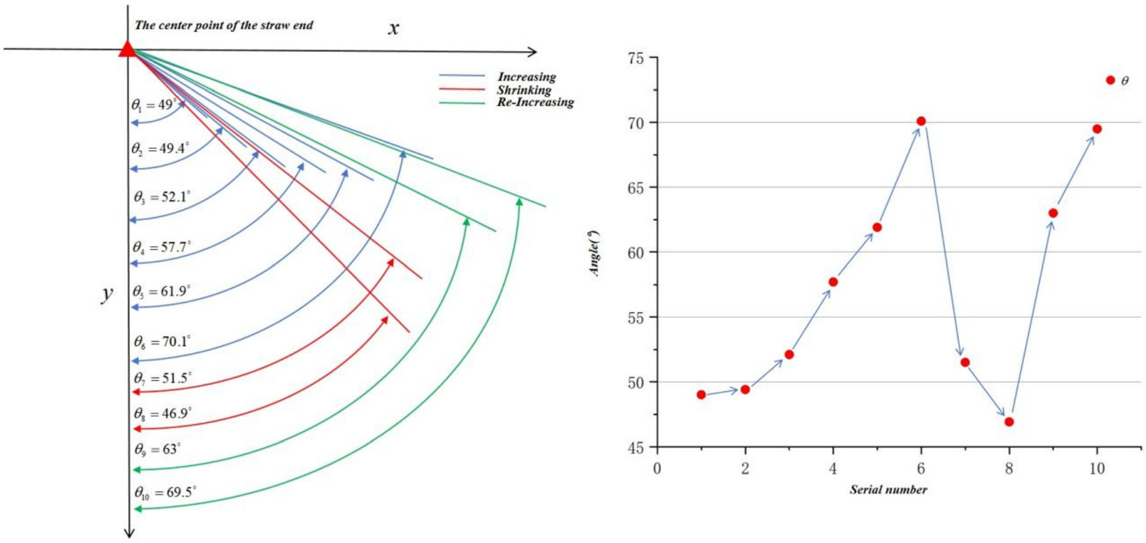

Change the diagram of the angle between the incident airflow and the central axis of the bubble when v=14 m/s

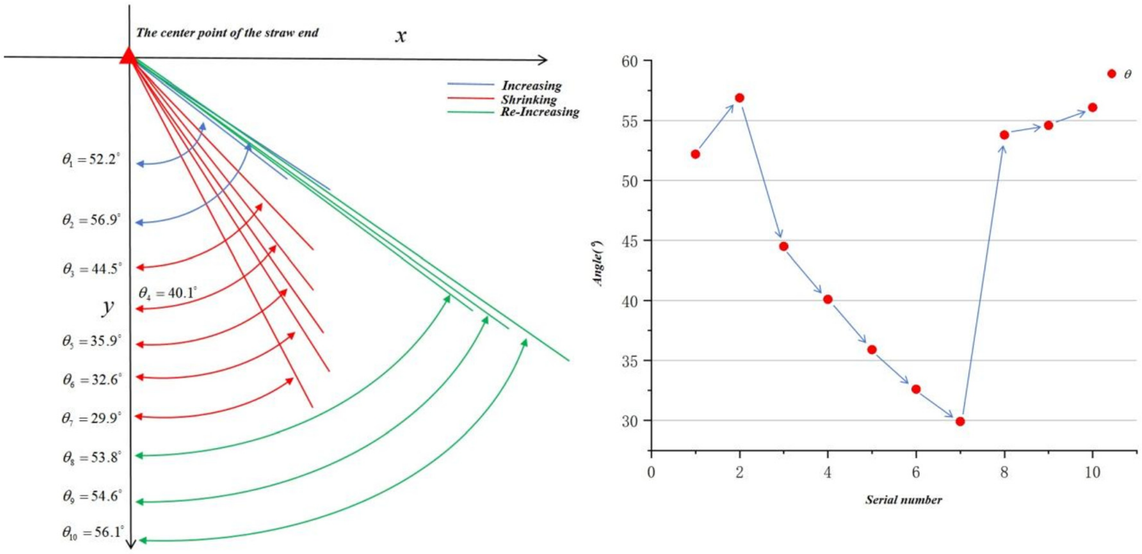

Change the diagram of the angle between the incident airflow and the central axis of the bubble when v=16 m/s

FIG. 17. Variation of incident airflow angle.

This experiment verifies the bubble growth model at low flow rates. The value of h is minimal and extremely difficult to measure. Therefore, this experiment determines the values of H_b and R_b through an identification program and then calculates the change process of h based on the relationship $h = 2R_b - H_b$ to compare it to the theoretical model.

Figure 20 shows that the incident velocity of the airflow has minimal influence on the value of h, affecting it only before 0.07 s. In

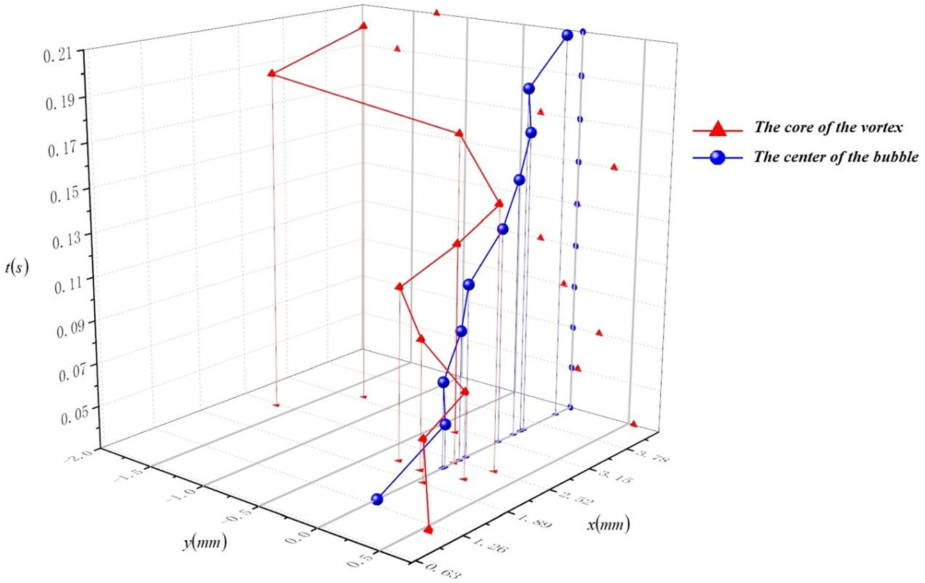

FIG. 18. Changes in the position of the vortex center point and bubble center over time.

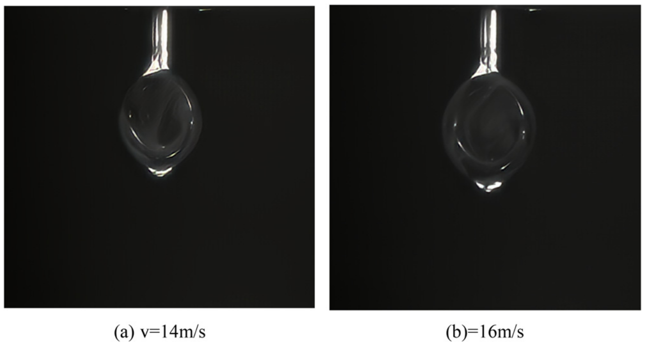

(a) v=14m/s

(b)=16m/s

FIG. 19. Left-handed vortex.

addition, the experimental values are generally consistent with the theoretical values, indicating that this theoretical model has a degree of rationality. At the stage where t is less than 0.07 s, the experimental results exhibit specific errors due to the inherent instability of the bubble.

C. The vortex inside the bubble at high flow speed

Before examining the high-speed incident airflow, let's briefly explain the case where the incident velocity is 18 m/s. When the incident velocity of the mixed gas is 18 m/s, the Reynolds number is approximately 2300, indicating that the gas in the straw transitions from laminar flow to turbulent flow. The airflow movement during this period is more complex, and the experimental observations reflect this complexity.

TABLE I. Statistics of the number of left-handed vortices at different speeds.

Pipe inner radius (mm)	1	2	4	6	8	10
$v = 14$ m/s	25	22	25	26	25	23
$v = 16$ m/s	26	30	25	31	24	25

Figure 21 indicates that when the incident velocity is 18 m/s, the flow field inside the bubble undergoes a relatively chaotic process. At $t = 0.13$ s, due to the high incident velocity, the incident airflow is visibly tilted in the vertical direction, and vortex structures appear on both sides of the incident airflow. This differs significantly from the internal structure of the bubble at lower speeds. As more incident airflow enters the bubble, the flow exhibits an unstable phenomenon of oscillating left and right, leading to typical chaos at $t = 0.17$ s. At $t = 0.21$ s, the structure inside the bubble becomes chaotic and blurred.

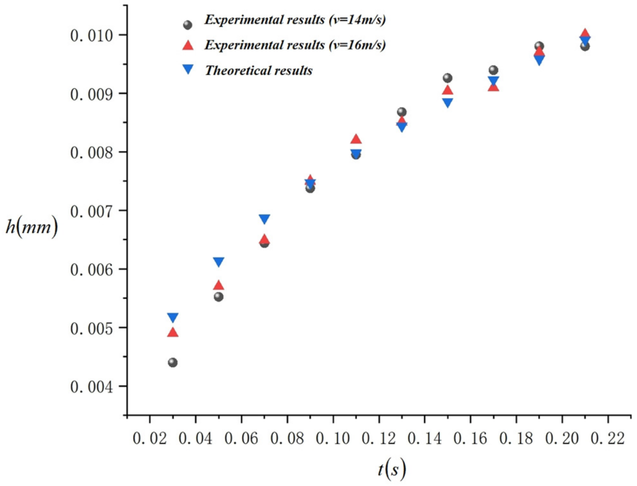

FIG. 20. Comparison of experimental and theoretical values of h at different speeds.

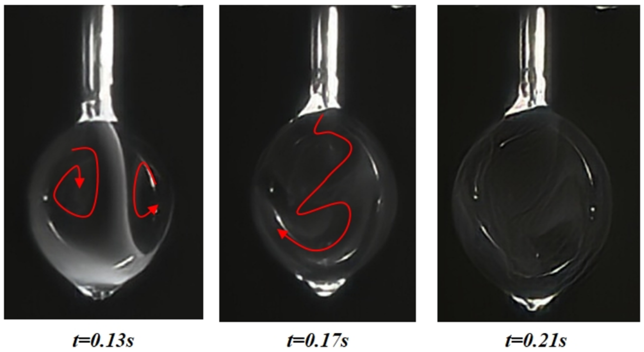

FIG. 21. Typical moments of the flow field inside a bubble when $v = 18$ m/s.

A four-vortex structure developed inside the bubble's flow field during the high-injection velocity experiment. However, the formation process of this structure gradually changed with increasing injection velocity.

When the incident velocity is 20 m/s, the flow field inside the bubble changes as follows:

Figure 22 demonstrates that when the mixed gas enters the bubble at the initial stage, Figs. 22(a)–22(c), the mixed gas velocity is relatively high and moves vertically toward the bottom of the bubble upon entry. Since the bubble wall exhibits considerable elasticity, the incident airflow reflects, forming a bilaterally symmetrical vortex structure. As more mixed gas enters the bubble, the vortex structures on the left and right sides gradually rise and expand. Simultaneously, the gas outside the vortex diffuses upward, as marked by the red arrow in Fig. 22(d). The mixed gas engulfs this diffused gas, rebounding from

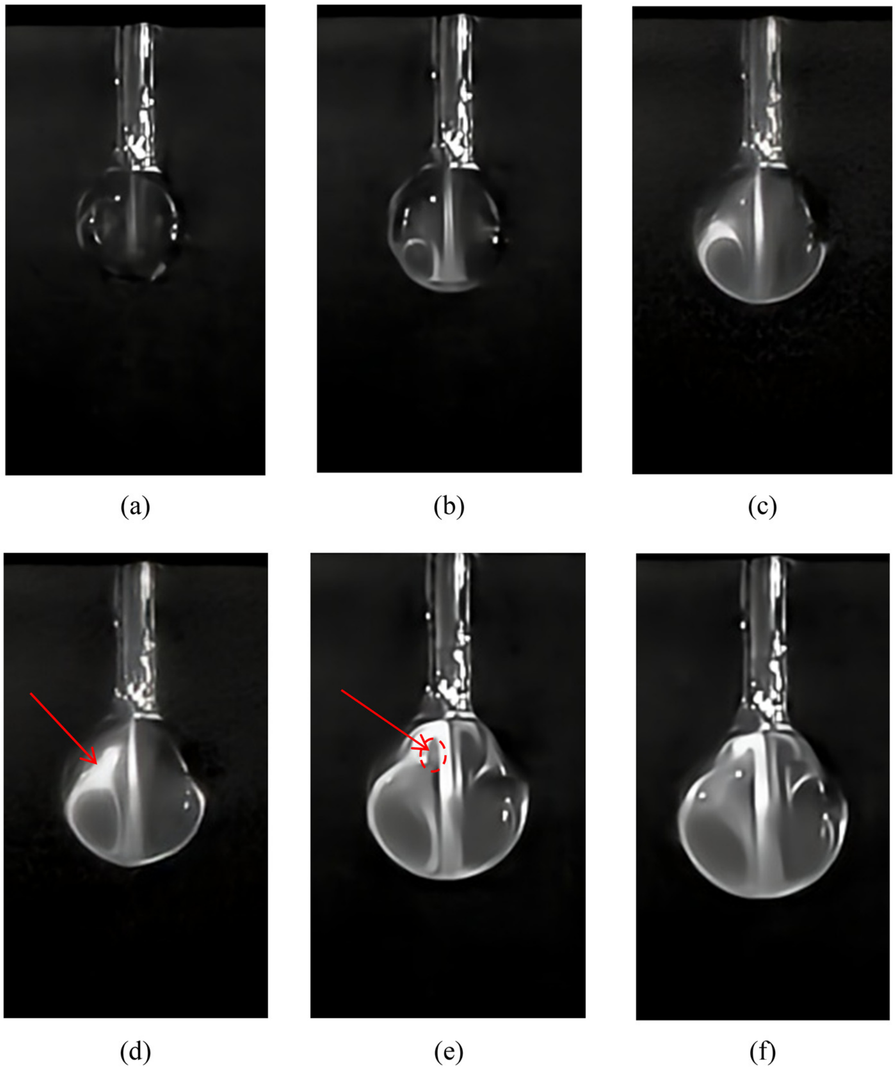

FIG. 22. Changes in the flow field inside the bubble when the incident velocity $v = 20$ m/s.

the bottom of the bubble and moving upward. Upon encountering the upper wall of the bubble, the gas rebounds a second time, forming the second vortex structure, marked by the dotted box in Fig. 22(e). At this stage, four symmetrical vortex structures around the bubble's centerline emerge inside the bubble. Then, the vortex structures blur and overlap due to the excessive quantity of mixed gas inside the bubble, showing a chaotic state in Fig. 22(f).

When the incident velocity is 22 m/s, the process slightly differs, and the flow field inside the bubble changes as follows:

Figure 23 indicates that when the incident airflow enters the bubble, it exhibits a vertical downward jet state. When the jet encounters the wall at the bottom of the bubble, its further development is hindered, forming two symmetrical vortex structures at the bottom, as depicted in Fig. 23(b). Then, the rebounded part of the jet changes direction to upward movement, causing the airflow to rise and diffuse, as shown in Fig. 23(c). When the rising airflow encounters the upper wall of the bubble, it rebounds for the second time, forming vortex structures Nos. 3 and 4 inside the bubble, as depicted in Fig. 23(d). At this stage, the flow field inside the bubble forms a four-vortex structure, and Figs. 23(e) and 23(f) illustrate the further development of this structure.

The study extracts the coordinate change process of the vortex structure's center point to demonstrate the development process of the vortex structure, with the results as follows:

Figure 24 demonstrates that this study extracts the central coordinate point of the vortex structure of the bubble. The original point represents the center point at the end of the straw, and the Vortexes 3 and 4 inside the bubbles appear later. The four vortices essentially represent the structure of the central line of the bubble. When Vortexes 1 and 2 appear, their positions are lower, and the centerline of the bubble is closer. As the mixed gas enters the bubbles, Vortexes 1 and 2 gradually expand, and the center point progressively rises. After reaching a certain level, Vortexes 3 and 4 are formed. The formation of these two suppresses the development of Vortexes 1 and 2. Hence, the center

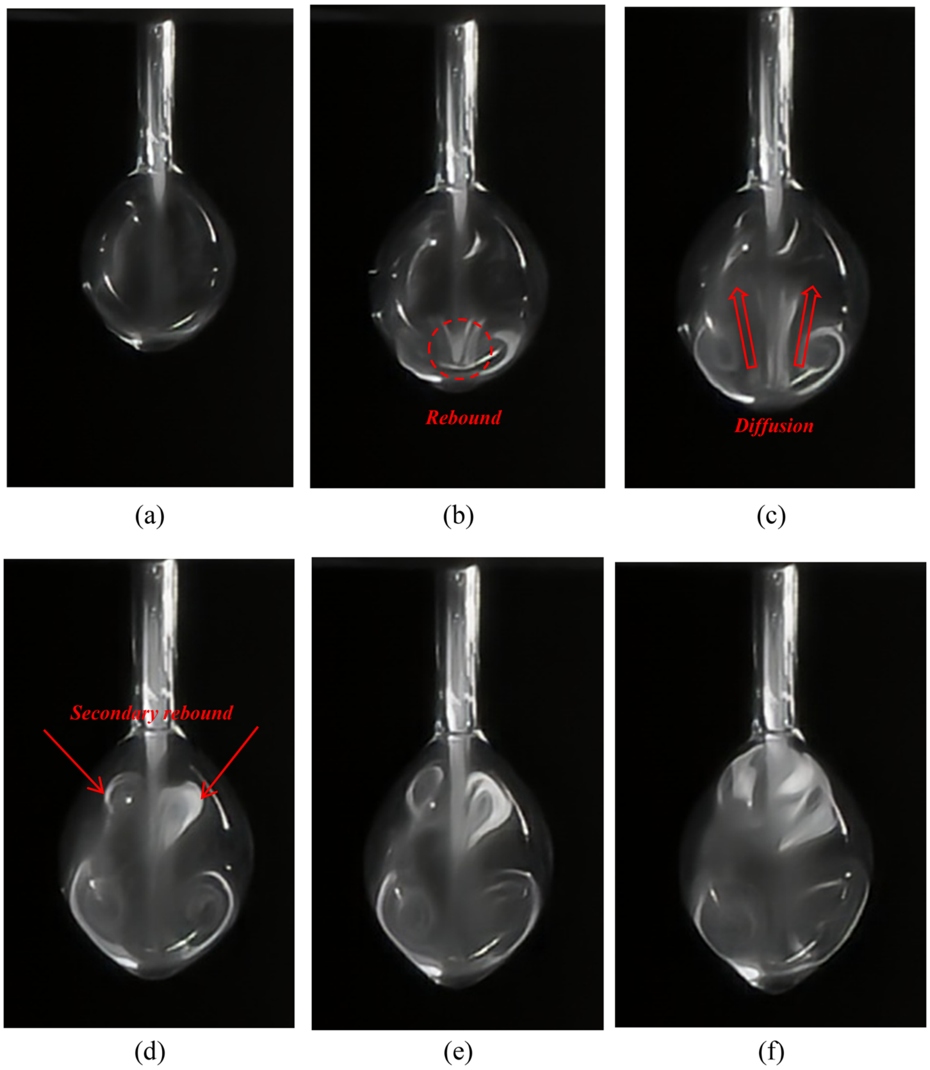

FIG. 23. Changes in the flow field inside the bubble when the incident velocity $v = 22$ m/s.

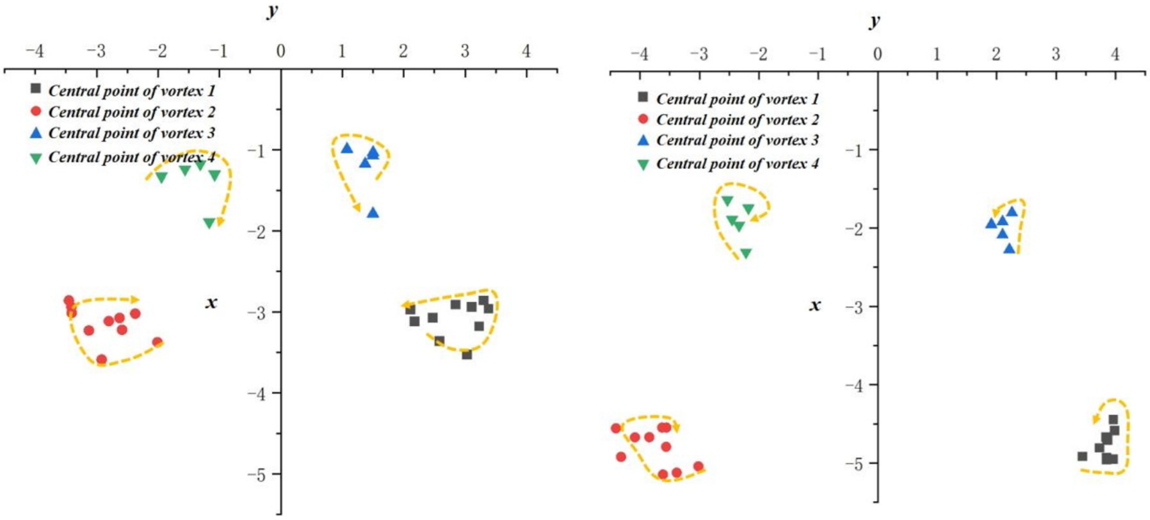

(a). V=20 m/s (b). V=22 m/s

FIG. 24. The central point coordinates change in the diagram at different speeds.

points of the latter exhibit a trend of slowly approaching the centerline of the bubble. Overall, the change in the center of the vortices is minimal, and the distribution is more concentrated.

For air bubble growth models under high current, Eqs. (9) and (10) remain applicable. However, when the speed exceeds 18 m/s, the flow inside the straw becomes turbulent, making Eq. (11) unsuitable for high-speed flow models. Therefore, modifications are necessary.

Calculating the friction loss of turbulence in the pipeline is highly challenging, as it is almost impossible to solve Δp in Eq. (7). Therefore, the study adopts the method of the loss coefficient in the ideal model. The ideal model addresses the velocity solution in Eq. (4). The speed at this stage is:

$$V_{indeal} = \sqrt{\frac{8\gamma}{\rho_g R_{in}}}. \tag{14}$$

This study assumes that the speed at the exit of the straw under a high current state is as follows:

$$v = kV_{ideal} = k\sqrt{\frac{8\gamma}{\rho_g R_{in}}}, \tag{15}$$

where k is the friction attenuation coefficient, which is determined experimentally. In the scenario where the straw does not dip into the soap liquid, the flow of the mixed gas is shown in Fig. 25:

The speed of the measurement point in this experiment was measured using TEMA software, and each speed was determined through 50 experiments. The speed of the measurement point in this study is v_m, $k = \frac{V_y}{v_m}$; the final k value represents the average of 50 experiments. After the measurement, when the speed is 20 m/s, $k = 0.90127$, and

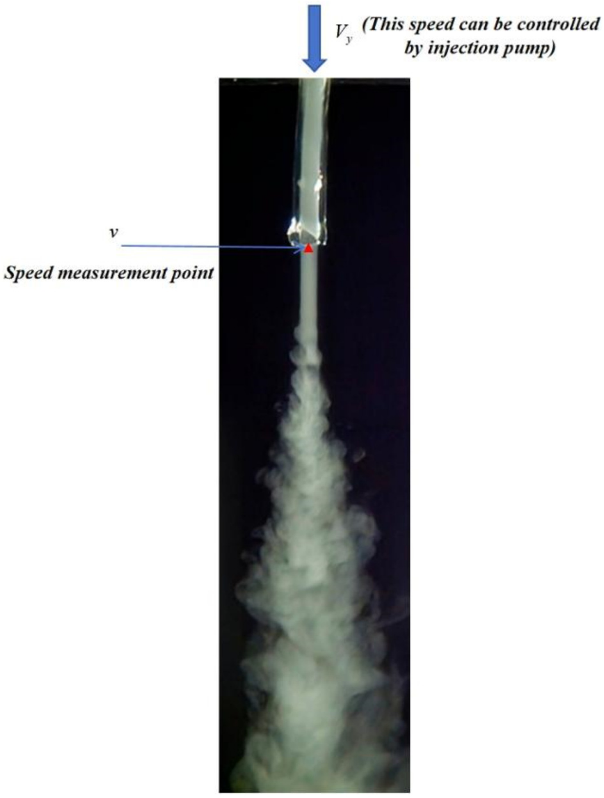

FIG. 25. Specification points schematic diagram.

when the speed is 22 m/s, $k = 0.90115$. The gap between the two values is very small, so in the final bubble model, $k = 0.90$.

After derivation, the change rate of h on time t is written as follows:

$$\frac{dh}{dt} = \frac{B}{R_{in}^2 + h^2}, \tag{16}$$

where $B = 3.6\sqrt{\frac{2\gamma}{\rho_g}} \cdot R_{in}^{\frac{3}{2}}$ and the form of Eqs. (16) and (12) maintain a high degree of consistency. Therefore, the relationship between h and t can finally be written as follows:

$$h^3 + 3R_{in}^2 h - 3Bt = 0. \tag{17}$$

Similarly, this study measures the entire change process of bubbles and verifies this model:

Figure 26 shows that the theoretical model is closely fitted with the experimental data, verifying the accuracy of the theoretical model within a specific range. The bubble growth rate at a speed of 22 m/s is slightly higher than that of the bubbles when the speed is 20 m/s.

IV. CONCLUSION

This study utilizes an independent laser observation device to examine the flow field within a soap bubble. It investigates the relationship between bubble formation and the speed of incident airflow at various transmission speeds and the correlation between changes in the flow field and the incident speed. In addition, this research proposes distinct mathematical and physical models for different stages of bubble formation. These models can more accurately calculate the minimum velocity for bubble formation and bubble growth at different Reynolds numbers, which has a certain reference significance for the research of soft robots and bubble dynamics. At the same time, in this study, we obtained the flow modes inside the bubbles. These vortex structures are surprisingly similar to the blood flow inside the heart, which may promote the development of artificial hearts. The following conclusions can be drawn:

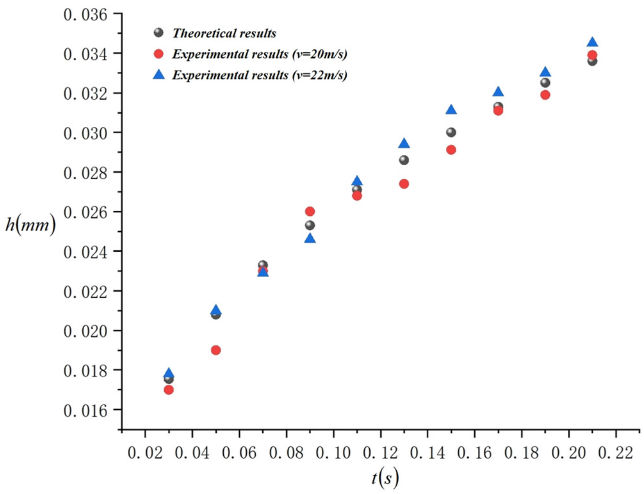

FIG. 26. The comparison of theoretical model and experimental results.

(1) Not all speeds can generate bubbles, as bubbles have a minimum speed threshold. This threshold can be determined through the proposed mathematical and physical model. In the initial generation of bubbles, the growth rate is relatively unstable and undergoes a shock process. This process shortens with the increase in ventilation rate, and the bubble growth rate stabilizes at a relatively constant value.

(2) When the airflow speed inside the straw is low, the internal flow exhibits a layered pattern. In this case, the streamlines inside the bubble show a single vortex structure. The angle between the incident airflow and the centerline of the bubble rises, decreases, and then increases again in three stages. The length of these stages is related to the speed of the incident airflow. As the speed increases, the first stage shortens while the lengths of the second and third stages grow. Simultaneously, the center point of the vortex inside the bubble is initially located near the geometric center of the bubble and then gradually moves away from it.

(3) When the airflow gradually increases and the flow inside the straw is in the rotation period, the Reynolds number gradually approaches the critical Reynolds number. The flow field inside the bubble becomes more chaotic, showing the phenomenon of left and right instability. When the airflow increases, the Reynolds number inside the straw exceeds the critical Reynolds number, and the flow becomes turbulent. At this time, the internal flow field of the bubbles exhibits a four-vortex structure. The formation of the four-vortex structure slightly varies with changes in the speed of the incident airflow. When the incident speed is 20 m/s, the formation of the four-vortex structure is primarily due to the proliferation of vortices. When the incident speed is 22 m/s, the formation of the four-vortex structure is mainly based on the rebound of the shooting.

ACKNOWLEDGMENTS

The authors would like to acknowledge the funding from the Hong Kong Polytechnic University and the Research Grants Council of the Hong Kong SAR (PolyU 15200323).

AUTHOR DECLARATIONS

Conflict of interest

The authors have no conflicts to disclose

Author Contributions

Qingkai Zhao: Conceptualization (equal); Formal analysis (lead); Methodology (lead); Visualization (equal); Writing – original draft (lead); Writing – review & editing (lead). **Zhixuan Yang:** Formal analysis (equal); Methodology (equal); Software (lead); Validation (equal); Visualization (lead). **Wei Xiao:** Data curation (equal); Resources (equal); Supervision (equal); Writing – review & editing (equal). **Ying Li:** Data curation (equal); Supervision (equal); Validation (lead); Writing – review & editing (equal). **Yatsze Choy:** Conceptualization (lead); Funding acquisition (lead); Project administration (lead); Resources (lead); Writing – review & editing (equal).

DATA AVAILABILITY

The data that support the findings of this study are available from the corresponding author upon reasonable request.

REFERENCES

[1] A. M. Zhang, X. L. Yao, and X. B. Yu, "The dynamics of three-dimensional underwater explosion bubble," J. Sound Vib. **311**(3–5), 1196–1212 (2008).

[2] J. Liu, W. Xiao, and X. Yao, "Pressure characteristics of a nonspherical underwater explosion bubble in a compressible fluid," Phys. Fluids **36**(5), 057145 (2024).

[3] C. L. Wu, N. N. Liu, Q. Wang, P. D. Zhao, P. N. Sun, and S. L. Yue, "Study on the jetting characteristics of an underwater explosion bubble collapsing near a floating body," Phys. Fluids **36**(10), 112641 (2024).

[4] B. A. Taha, A. J. Addie, A. J. Haider, A. C. Kadhim, A. S. Azzahrani, and N. Arsad, "Needle-free targeted injections using bubble laser technology in therapeutics," Langmuir **40**(44), 23549–23561 (2024).

[5] Y. Jin, T. Zhang, Y. Yang, H. Chen, Y. Li, and H. Wu, "How the texture density affect dynamics of a single acoustic cavitation bubble near a skin-like wall in sonophoresis applications," IEEE Access **12**, 34505–34511 (2024).

[6] V. Bulycheva, M. C. Kolios, and R. Karshafian, "Interaction of ultrasonically driven bubble with a soft tissue-like boundary," Ultrasonics **142**, 107374 (2024).

[7] P. A. Amendt, M. Strauss, R. A. London *et al.*, "Modeling of bubble dynamics in relation to medical applications," Laser-Tissue Interact. VIII. SPIE **2975**, 362–373 (1997).

[8] L. Bourgois, D. Delacroix, and A. Ostrowsky, "Use of bubble detectors to measure neutron contamination of a medical accelerator photon beam," Radiat. Prot. Dosim. **74**(4), 239–246 (1997).

[9] K. Yasui, T. Tuziuti, M. Sivakumar, and Y. Iida, "Theoretical study of single-bubble sonochemistry," J. Chem. Phys **122**(22), 224706 (2005).

[10] C. Kalmár, K. Klapcsik, and F. Hegedűs, "Relationship between the radial dynamics and the chemical production of a harmonically driven spherical bubble," Ultrason. Sonochem. **64**, 104989 (2020).

[11] D. Qin, S. Lei, B. Zhang, Y. Liu, J. Tian, X. Ji, and H. Yang, "Influence of interactions between bubbles on physico-chemical effects of acoustic cavitation," Ultrason. Sonochem. **104**, 106808 (2024).

[12] M. Ali and J. H. He, "Bipolymer nanofibers: Engineering nanoscale interface via bubble electrospinning," J. Appl. Polym. Sci **141**(5), e54878 (2024).

[13] W. Chirwa, P. Li, H. Zhan, Y. Zhang, and Y. Liu, "Application of fine bubble technology toward sustainable agriculture and fisheries," J. Cleaner Prod. **449**, 141629 (2024).

[14] Y. Z. Liu, S. F. Ren, and P. F. Zhao, "Application of the deep neural network to predict dynamic responses of stiffened plates subjected to near-field underwater explosion," Ocean Eng. **247**, 110537 (2022).

[15] S. F. Ren, P. F. Zhao, S. P. Wang, and Y. Z. Liu, "Damage prediction of stiffened plates subjected to underwater contact explosion using the machine learning-based method," Ocean Eng. **266**, 112839 (2022).

[16] X. Wang, S. Li, J. Shen, H. Bian, G. Wu, Y. Zhang, Q. Jiang, J. Li, and Y. Zhang, "Dynamic behaviors of a bubble near a rectangular wall with a bulge," Phys. Fluids **36**(2), 02334 (2024).

[17] Y. Fan, T. Chen, G. Yang, X. Cui, W. Lu, G. Wang, and B. Tian, "Experimental investigation on dynamic response of concrete gravity dam under shock wave and bubble pulsation," Eng. Struct. **318**, 118796 (2024).

[18] J. Magnaudet and G. Mougin, "Wake instability of a fixed spheroidal bubble," J. Fluid Mech. **572**, 311–337 (2007).

[19] B. Yang and A. Prosperetti, "Linear stability of the flow past a spheroidal bubble," J. Fluid Mech. **582**, 53–78 (2007).

[20] Q. Zhao, W. Xiao, X. Yao, K. Han, and X. Chen, "Experimental study on flow characteristics of cavitation bubbles in underwater vertical movement of double vehicles," Ocean Eng. **260**, 111940 (2022).

[21] M. S. Plesset and R. B. Chapman, "Collapse of an initially spherical vapour cavity in the neighbourhood of a solid boundary," J. Fluid Mech. **47**(2), 283–290 (1971).

[22] W. Lauterborn and H. Bolle, "Experimental investigations of cavitation-bubble collapse in the neighbourhood of a solid boundary," J. Fluid Mech. **72**(2), 391–399 (1975).

[23] S. Li, Y. Zhang, and F. G. Hammitt, "Characteristics of cavitation bubble collapse pulses, associated pressure fluctuations, and flow noise," J. Hydraul. Res. **24**(2), 109–122 (1986).

[24] O. Lindau and W. Lauterborn, "Cinematographic observation of the collapse and rebound of a laser-produced cavitation bubble near a wall," J. Fluid Mech. **479**, 327–348 (2003).

[25] R. W. Kermeen, J. T. McGraw, and B. R. Parkin, "Mechanism of cavitation inception and the related scale-effects problem," J. Fluids Eng. **77**(4), 533–540 (1955).

[26] J. R. Blake and D. C. Gibson, "Cavitation bubbles near boundaries," Annu. Rev. Fluid Mech. **19**(1), 99–123 (1987).

[27] P. B. Robinson and J. R. Blake, "Dynamics of cavitation bubble interactions," in *Bubble Dynamics and Interface Phenomena: Proceedings of an IUTAM Symposium Held, Springer Netherlands, Dordrecht, 6–9 September 1993,* edited by J. R. Blake, J. M. Boulton-Stone, N. H. Thomas (Springer Netherlands, Dordrecht, 1994), pp. 55–64.

[28] A. M. Zhang and Y. L. Liu, "Improved three-dimensional bubble dynamics model based on boundary element method," J. Comp. Phys. **294**, 208–223 (2015).

[29] A. Hanke and R. Metzler, "Bubble dynamics in DNA," J. Phys. A: Math. Gen. **36**(36), L473–L480 (2003).

[30] Y. Zhou, P. Kang, Z. Huang, P. Yan, J. Sun, J. Wang, and Y. Yang, "Experimental measurement and theoretical analysis on bubble dynamic behaviors in a gas-liquid bubble column," Chem. Eng. Sci. **211**, 115295 (2020).

[31] R. Mettin, C. Cairós, and A. Troia, "Sonochemistry and bubble dynamics," Ultrason. Sonochem. **25**, 24–30 (2015).

[32] K. N. Huang, W. Xiao, X. L. Yao, and J. L. Liu, "Numerical investigation on cavity dynamics of water-entry bodies with different shape parameters," Phys. Fluids **35**, 062115 (2023).

[33] W. Xiao, A. M. Zhang, X. Ye, and L. Q. Sun, "Numerical investigation of toroidal bubble dynamics in a compressible fluid based on boundary integral method," Phys. Fluids **31**(10), 107106 (2019).

[34] T. H. Phan, E. Kadivar, V. T. Nguyen, O. el Moctar, and W. G. Park, "Thermodynamic effects on single cavitation bubble dynamics under various ambient temperature conditions," Phys. Fluids **34**(2), 023318 (2022).

[35] Y. Shen, K. Yasui, T. Zhu, and M. Ashokkumar, "A model for the effect of bulk liquid viscosity on cavitation bubble dynamics," Phys. Chem. Chem. Phys. **19**(31), 20635–20640 (2017).

[36] C. Huber, Y. Su, C. T. Nguyen, A. Parmigiani, H. M. Gonnermann, and J. Dufek, "A new bubble dynamics model to study bubble growth, deformation, and coalescence," JGR Solid Earth **119**(1), 216–239 (2014).

[37] J. Straub, "Boiling heat transfer and bubble dynamics in microgravity," Adv. Heat Trans. **35**, 57–172 (2001).

[38] X. Zhong and A. M. Ardekani, "A model for bubble dynamics in a protein solution," J. Fluid Mech. **935**, A27 (2022).

[39] T. Ahmed and B. D. Erath, "Experimental study of vortex ring impingement on concave hemispherical cavities," J. Fluid Mech. **967**, A38 (2023).

[40] S. J. Rao, S. Jain, and S. Basu, "Dynamics of soap bubble inflation," Phys. Rev. Fluids **9**(5), L051602 (2024).

[41] Y. Li and Y. S. Choy, "Acoustic behaviour of micro-perforated panel backed by shallow cavity under fully developed grazing flow," J. Sound Vib. **569**, 117985 (2024).

[42] Y. Li and Y. S. Choy, "Broadband and low-frequency sound absorption of compact meta-liner under grazing flow," Appl. Acoust. **224**, 110146 (2024).

[43] Q. Xi, Y. S. Choy, L. Cheng, and S. K. Tang, "Noise control of dipole source by using micro-perforated panel housing," J. Sound Vib. **362**, 39–55 (2016).

[44] H. S. Zhen, C. S. Cheung, C. W. Leung, and Y. S. Choy, "A comparison of the emission and impingement heat transfer of LPG–H_2 and CH_4–H_2 premixed flames," Int. J. Hydrogen Energy **37**(14), 10947–10955 (2012).

[45] S. Wang, Z. Qiao, Z. Li *et al.*, "Jellyfish-inspired soft robot driven by pneumatic bistable actuators," Soft Rob. (2024).

[46] T. T. Nguyen and D. Q. Nguyen, "Soft robot employing a series of pneumatic actuators and distributed balloons: Modeling, evaluation, and applications," IEEE Trans. Rob. **40**, 3933 (2024).

[47] G. Monreal, S. C. Koenig, J. Huang *et al.*, "Anatomical and hemodynamic characterization of totally artificial hearts," ASAIO J. **70**(5), 338–347 (2024).

[48] F. Zhao, Z. Wen, X. Gu, W. Zhang, and X. Tang, "Operando gas- and particle-phase measurements of combustion cigarette smoke aerosols by vacuum ultraviolet photoionization mass spectrometry," J. Aerosol Sci. **178**, 106358 (2024).

[49] L. Zeng, H. Wang, Y. Li, and X. He, "Measurement for the thickness of water droplets/film on a curved surface with digital image projection (DIP) technique," Sens. (Basel) **20**(8), 2409 (2020).

[50] R. Shen, Y. Deng, B. Li, X. Li, J. Xu, and H. Wang, "Measuring and modeling detachment characteristics of onset bubbles via image processing," Chem. Eng. Res. Des. **203**, 406–418 (2024).

[51] Q. Zhao, T. Chen, W. Xiao, X. Chen, X. Yao, and W. Wang, "Research on the characteristics of cavitation flow and pressure load during vertical water exit of different head-shaped vehicles," Ocean Eng. **265**, 112663 (2022).

[52] L. Salkin, A. Schmit, P. Panizza, and L. Courbin, "Generating soap bubbles by blowing on soap films," Phys. Rev. Lett. **116**(7), 077801 (2016).

[53] M. Zhou, M. Li, Z. Chen, J. Han, and D. Liu, "Formation of soap bubbles by gas jet," Appl. Phys. Lett. **111**(24), 241604 (2017).

[54] H. Darcy, *Les Fontaines Publiques de la Ville de Dijon: Exposition et Application Des Principes à Suivre et Des Formules à Employer Dans Les Questions de Distribution D'eau* (Victor Dalmont, 1856), pp. 647.